

## NRC Publications Archive Archives des publications du CNRC

### **Self-calibrating aerosol absorption measurements using co-located TDLAS and tunable-wavelength photothermal interferometry**

Corbin, Joel C.; Moallemi, Alireza; Poitras, Daniel; Sipkens, Timothy A.; Norooz Oliaee, Jalal

This publication could be one of several versions: author's original, accepted manuscript or the publisher's version. / La version de cette publication peut être l'une des suivantes : la version prépublication de l'auteur, la version acceptée du manuscrit ou la version de l'éditeur.

For the publisher's version, please access the DOI link below. / Pour consulter la version de l'éditeur, utilisez le lien DOI ci-dessous.

#### **Publisher's version / Version de l'éditeur:**

<https://doi.org/10.1080/02786826.2025.2469780>

*Aerosol Science and Technology*, pp. 1-15, 2025-03-07

#### **NRC Publications Archive Record / Notice des Archives des publications du CNRC :**

<https://nrc-publications.canada.ca/eng/view/object/?id=6da5f946-0b08-41d8-8f84-e9f6cbcc49b0>

<https://publications-cnrc.canada.ca/fra/voir/objet/?id=6da5f946-0b08-41d8-8f84-e9f6cbcc49b0>

Access and use of this website and the material on it are subject to the Terms and Conditions set forth at

<https://nrc-publications.canada.ca/eng/copyright>

READ THESE TERMS AND CONDITIONS CAREFULLY BEFORE USING THIS WEBSITE.

L'accès à ce site Web et l'utilisation de son contenu sont assujettis aux conditions présentées dans le site

<https://publications-cnrc.canada.ca/fra/droits>

LISEZ CES CONDITIONS ATTENTIVEMENT AVANT D'UTILISER CE SITE WEB.

**Questions?** Contact the NRC Publications Archive team at

PublicationsArchive-ArchivesPublications@nrc-cnrc.gc.ca. If you wish to email the authors directly, please see the first page of the publication for their contact information.

**Vous avez des questions?** Nous pouvons vous aider. Pour communiquer directement avec un auteur, consultez la première page de la revue dans laquelle son article a été publié afin de trouver ses coordonnées. Si vous n'arrivez pas à les repérer, communiquez avec nous à PublicationsArchive-ArchivesPublications@nrc-cnrc.gc.ca.



## Self-calibrating aerosol absorption measurements using co-located TDLAS and tunable-wavelength photothermal interferometry

Joel C. Corbin, Alireza Moallemi, Daniel Poitras, Timothy A. Sipkens & Jalal Norooz Oliiae

To cite this article: Joel C. Corbin, Alireza Moallemi, Daniel Poitras, Timothy A. Sipkens & Jalal Norooz Oliiae (07 Mar 2025): Self-calibrating aerosol absorption measurements using co-located TDLAS and tunable-wavelength photothermal interferometry, Aerosol Science and Technology, DOI: [10.1080/02786826.2025.2469780](https://doi.org/10.1080/02786826.2025.2469780)

To link to this article: <https://doi.org/10.1080/02786826.2025.2469780>



© 2025 The Author(s). Published with license by Taylor & Francis Group, LLC



Published online: 07 Mar 2025.



Submit your article to this journal [↗](#)



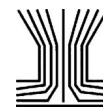
Article views: 84



View related articles [↗](#)



View Crossmark data [↗](#)



# Self-calibrating aerosol absorption measurements using co-located TDLAS and tunable-wavelength photothermal interferometry

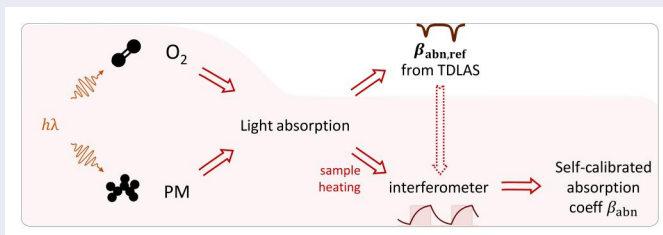
Joel C. Corbin<sup>a</sup> , Alireza Moallemi<sup>a</sup> , Daniel Poitras<sup>b</sup> , Timothy A. Sipkens<sup>a</sup> , and Jalal Norooz Oliae<sup>a</sup>

<sup>a</sup>Metrology Research Centre, National Research Council Canada, Ottawa, Ontario, Canada; <sup>b</sup>Quantum and Nanotechnologies Research Centre, National Research Council Canada, Ottawa, Ontario, Canada

## ABSTRACT

Photothermal spectroscopy, and photothermal interferometry (PTI) in particular, has the potential to provide reference measurements of aerosol absorption coefficients  $\beta_{\text{abn}}$ . Such  $\beta_{\text{abn}}$  measurements represent a fundamental property of aerosols such as black carbon and brown carbon, the accurate knowledge of which is essential for understanding their climate forcing;  $\beta_{\text{abn}}$  can be used in calculating the imaginary refractive index, absorption function, or mass absorption cross-section of a sample. Furthermore,  $\beta_{\text{abn}}$  is commonly expressed in units of equivalent black carbon mass (eBC) in the many photoacoustic or filter-based instruments that are used for air-quality monitoring and emissions testing of on-road, airborne, and marine transportation. Here, we propose the use of tunable-laser PTI (TL-PTI) as a self-calibrating reference technique for quantifying  $\beta_{\text{abn}}$ . In TL-PTI, a wavelength-tunable laser is used to quantify the narrow absorption lines of a gas *via* direct absorption spectroscopy, providing a reference  $\beta_{\text{abn,ref}}$  in units of  $\text{Mm}^{-1}$ . The A-band absorption lines of ambient oxygen at about 760 nm provide a convenient reference. The PTI signal is then calibrated to this  $\beta_{\text{abn,ref}}$ . This gas-PTI signal can then be “switched off” by tuning the laser wavelength away from the absorption lines, so that only particulate PTI signals remain in the background-subtracted signal. The PTI signal is directly related to light absorption for both aerosols and gases, since the PTI pump-laser modulation is slower than the thermalization timescales of both. We demonstrate the accuracy of our PTI prototype by retrieving the refractive index of nigrosine dye.

## GRAPHICAL ABSTRACT



## ARTICLE HISTORY

Received 18 October 2024  
Accepted 21 January 2025

## EDITOR

Hans Moosmüller

## 1. Introduction

Visible and infrared light absorption by nanoparticles such as soot, graphene, metals, and dust underlies key processes and measurements in combustion, materials synthesis, climate, and medicine. Light absorption by airborne soot results in climate forcing which is comparable to that of  $\text{CO}_2$  and which continues after deposition onto snow and ice (Ramanathan and Carmichael 2008). Light absorption by graphene, reduced graphene

oxide, or other synthetic nanoparticles can be exploited to develop the production of such materials for industrial applications (Daun et al. 2017; Musikhin et al. 2021). Finally, light absorption by metallic nanoparticles can be used to determine their size for various applications in spectroscopy, sensing, and fabrication (Sipkens et al. 2022; Willets and Van Duyne 2007). The airborne measurement of nanoparticle light absorption is therefore of broad scientific value.

**CONTACT** Joel C. Corbin Joel.Corbin@nrc-cnrc.gc.ca Metrology Research Centre, National Research Council of Canada, 1200 Montreal Road, Ottawa, ON, K1A 0R6, Canada.

© 2025 The Author(s). Published with license by Taylor & Francis Group, LLC

This is an Open Access article distributed under the terms of the Creative Commons Attribution-NonCommercial-NoDerivatives License (<http://creativecommons.org/licenses/by-nc-nd/4.0/>), which permits non-commercial re-use, distribution, and reproduction in any medium, provided the original work is properly cited, and is not altered, transformed, or built upon in any way. The terms on which this article has been published allow the posting of the Accepted Manuscript in a repository by the author(s) or with their consent.

Nanoparticle light absorption is generally broadband, with spectral features spanning hundreds of nanometers for most carbonaceous materials (Corbin et al. 2019; Sun, Biedermann, and Bond 2007), and tens of nanometers of wavelength even for extreme cases of quantum dots (Won et al. 2019). In contrast, small gas molecules display distinct and relatively narrow absorption “lines” with sub-nanometer widths. The precise widths of these gas absorption lines expand slightly with increasing temperature and pressure.

Due to the broadband nature of aerosol light absorption, most measurement devices utilize a few select wavelengths, rather than being highly spectrally resolved. For example, three to seven wavelengths are used in some filter-based photometers which estimate light absorption from the light attenuation of a particle-laden filter (Lack et al. 2014; Moosmüller, Chakrabarty, and Arnott 2009). More-direct measurements of light absorption can be made using photoacoustic spectroscopy, in which a modulated excitation laser heats aerosols to generate acoustic waves whose power correlates with the aerosol absorption coefficient  $\beta_{\text{abn}}$  (Al Fischer and Smith 2018; Arnott, Moosmüller, and Walker 2000; Lack et al. 2006; Moosmüller, Chakrabarty, and Arnott 2009; Schnaiter et al. 2023; Stylogiannis et al. 2021). These acoustic waves are typically detected by a microphone, although a significant enhancement in sensitivity has been realized using novel transducers such as quartz tuning forks (Ma 2020; Patimisco et al. 2014) or cantilever for detection (Karhu et al. 2022; Koskinen et al. 2008). Many other PAS configurations are possible (Haisch 2012). Notably, advanced techniques such as beat-frequency quartz-enhanced PAS (Wu et al. 2017) allow for high-sensitivity and calibration-free gas monitoring.

Other approaches to the measurement of aerosol light absorption also exist. In particular, the extinction-minus-scattering (EMS) approach allows for the accurate calibration of aerosol light absorption in highly-absorbing samples (Modini et al. 2021). This approach is limited, however, by uncertainties related to the subtraction of two large numbers, and by a need to model the phase function of the measured particles in order to correct for unmeasured (“truncated”) scattering angles. This scattering angle error could be reduced substantially with specialized nephelometer designs (Varma, Moosmüller, and Arnott 2003), but this results in the need for two independent measurements and introduces undesirable uncertainty as well as complexity. Filter-based

photometers have also been developed which combine measurements of light extinction-and-scattering with radiative transfer calculations (Hyvärinen et al. 2013; Petzold and Schönlinner 2004), or which estimate absorption from measurements of light extinction (Lack et al. 2014; Sipkens et al. 2023). Such photometers allow for the realization of low-maintenance, low-cost devices suitable for air-quality monitoring networks. However, they are cross-sensitive to light scattering signals, such that their signals depend on the ratio of light-scattering to extinction (single-scattering albedo; SSA) as well as particle size (Drinovec et al. 2022; Nakayama et al. 2010).

Alternatively, photothermal spectroscopy (PTS) can be used to measure  $\beta_{\text{abn}}$  (Bialkowski, Astrath, and Proskurnin 2019). In PTS, the change of refractive index due to local sample heating is measured, rather than acoustic waves emanating from the sample. PTS and PAS are commonly treated as distinct techniques for this reason, although acoustic effects can be observed in PTS (Bialkowski, Astrath, and Proskurnin 2019). In aerosol and gas applications, the most common realization of PTS is photothermal interferometry (PTI). Relative to PAS, PTI removes the need for a resonant cell, which allows for a wider variety of measurement configurations (Krzempek et al. 2018; Radeschnig, Bergmann, and Lang 2024) and which significantly simplifies the use of multiple lasers to obtain spectrally resolved measurements of  $\beta_{\text{abn}}$  (Lewis et al. 2008). The lack of an acoustic resonator allows PTI sample cells to be optimized purely for aerosol transport, calibration (discussed below), or miniaturization (Radeschnig, Bergmann, and Lang 2024). It also allows any arbitrary excitation-laser modulation frequency to be used, in contrast to the requirement to match the resonance frequency of a quartz tuning fork (e.g., 33 kHz [Wu et al. 2017]) or acoustic cell (e.g.,  $\sim 1.5$  kHz [Arnott, Moosmüller, and Walker 2000; Gillis, Havey, and Hodges 2010]) in most PAS applications, as well as in tuning-fork-based thermoelastic spectroscopy (e.g., 6 kHz; Qiao et al. 2023). However, the absolute calibration of PTI measurements to  $\beta_{\text{abn}}$  remains an important issue, and is the focus of the current work.

Here, we propose the use of a tunable-wavelength laser to result in a self-calibrating tunable-laser PTI (TL-PTI) design. This laser is chosen such that it can be scanned across the absorption lines of a convenient gas molecule, such as  $\text{O}_2$ , while also corresponding to a wavelength absorbed by many nanoparticles of interest, such as 760 nm. Thus, tunable-diode-laser absorption spectroscopy (TDLAS) can be used,

independently of the interferometer, to provide a reference gas absorption coefficient  $\beta_{\text{abn,ref}}$  for calibration. The TDLAS signal is compared with the PTI signal obtained for the same gas absorption line for HEPA-filtered air, to calibrate the PTI interferometer. The aerosol PTI signal (and any background signals) is then measured by tuning the excitation laser away from the absorption line. This approach allows for an internal cross-calibration of the TL-PTI by changing only the laser wavelength, minimizing uncertainty in  $\beta_{\text{abn}}$ .

Below, we demonstrate this concept using a prototype system. We verify linearity in our measured  $\beta_{\text{abn}}$  by varying the excitation-laser power. We discuss the role of relaxation timescales for  $\text{O}_2$  and aerosols, which must both be smaller than the period of the excitation-laser modulation if signals from the two to be compared. We demonstrate the use of PTI combined with particle-volume measurements to retrieve the imaginary refractive index of nigrosine nanoparticles. Finally, we discuss our approach in the context of other instruments and calibration schemes.

## 2. Methods

### 2.1. Light absorption and optical depth

Light extinction can be described in terms of optical thickness  $\tau$  using the Beer-Lambert law (Arnott, Moosmüller, and Walker 2000),

$$\tau = -\ln\left(\frac{I}{I_0}\right) = \beta_{\text{ext}}l, \quad (1)$$

where  $\tau$  is described in terms of the intensity change from  $I_0$  to  $I$  for light passing through the sample; or equivalently in terms of a path length  $l$  and extinction coefficient  $\beta_{\text{ext}}$ .

For light-absorbing gases, which scatter light negligibly,  $\beta_{\text{ext}}$  becomes equivalent to the extinction coefficient  $\beta_{\text{abn}}$  so that  $\tau \approx A$ , the absorbance, so that Equation (1) is sometimes written as,

$$A = \beta_{\text{abn}}l. \quad (2)$$

Equation (2) also describes light absorption by small nanoparticles, which scatter light negligibly when at least tenfold smaller than the light wavelength. More precisely, this occurs when the size parameter  $x = \pi d/\lambda \ll 1$ , (Moosmüller and Arnott 2009) and when the particles are optically soft,  $x|m| \ll 1$  (where  $d$  is a particle diameter and  $m = n + ik$  is the complex refractive index of the particle) such that the electromagnetic field is uniform within the particles (Bohren 1986; Sorensen 2001). For particles with large

$d$  or large  $x|m|$ , light scattering  $\beta_{\text{sca}}$  must be considered ( $\beta_{\text{ext}} = \beta_{\text{abn}} + \beta_{\text{sca}}$ ).

### 2.2. Tunable diode laser absorption spectroscopy (TDLAS)

Tunable-diode laser absorption spectroscopy (TDLAS) is a technique wherein the wavelength  $\lambda$  of a diode laser is scanned by scanning the electrical current driving the laser, in order to measure the absorption features of a sample (Werle 1998). The use of a tunable diode laser (TDL) for this wavelength scan is not essential, but is practically convenient, as diode lasers are affordable and compact. Typically, increasing the TDL current above the diode's threshold current corresponds to a near-linear change in both wavelength  $\lambda$  (as intended) and laser intensity  $I_0$  (unintended). Precise TDLAS measurements require careful analysis to quantify the laser performance, and to account for any unintended changes in  $I_0$  during the  $\lambda$  scan. In particular, the voltage observed at a photodetector after the TDL must be fitted to determine the positively sloping baseline (due to drift in  $I_0$ ), the absorption lines of an analyte gas, and to fine-tune the wavelength response of the laser to current. The approximate wavelength of the laser must be known prior to the fit, and was determined in our case by tuning across multiple absorption peaks and comparing the result with the high-resolution transmission molecular absorption (HITRAN) database (Gordon et al. 2022; Yu, Drouin, and Miller 2014).

Gas absorption lines appear as Lorentzian peaks in TDLAS due to temperature and pressure broadening, and can be fitted by a function which includes these peaks and any baseline effects including drift in TDL wavelength and fluctuations in the  $\tau$  of the sample cell windows. We used the following equation for this fit (Norooz Oliaee et al. 2022; Rothman et al. 1998):

$$V(t_i) = V_0 + V_1 \exp[-\beta_{\text{abn}}(t_i)l_g], \quad (3)$$

where  $V(t_i)$  is the photodetector voltage measured from the TDL (in volts) at a time interval  $t_i$ ;  $V_0$  is the photodetector zero voltage, measured at a TDL current below the TDL threshold current; and  $V_1 = a_1 + a_2 t_i + a_3 t_i^2$  represents a near-linear baseline with coefficients  $a_1$ ,  $a_2$ ,  $a_3$  (the quadratic term  $a_3$  is typically small), and  $l_g$  is the absorption pathlength. Here,  $\beta_{\text{abn}}(t_i)$  is specified as a function of time because the TDL wavelength is scanned across the absorption peak over time.

$\beta_{\text{abn}}(t_i)$  is further described as a function of the partial pressure of the reference gas  $p_g$  (in atm), which

is unknown prior to the fit; the measured air temperature  $T_g$  (in Kelvin); and the Boltzmann constant (in J/K)  $k_B$ ,

$$\beta_{\text{abn}}(t_i) = \frac{p_g}{k_B T_g} \sum_j S_j \frac{1}{\pi} \frac{\gamma_j}{(v_i - v_{ij})^2 + \gamma_j^2}, \quad (4)$$

where the summation over indices  $j$  represents the total  $\lambda$ -dependent optical thickness due to Lorentzian gas absorption lines. In this summation,  $S_j$  are spectral line intensities (in cm/molecule),  $v_i$  is the wavenumber of the TDL at time  $t_i$ ,  $v_{ij} = 1/\lambda_j$  are transition wavenumbers, and  $\gamma_j$  are the pressure-broadening half-widths (in  $\text{cm}^{-1}$ ). These half-widths are represented by

$$\gamma_j = b_{\text{air}}(P - p_g) + b_{\text{self}}(p_g), \quad (5)$$

where  $b_{\text{self}}$  and  $b_{\text{air}}$  are self-broadening and air-broadening coefficients from HITRAN, respectively, which are dependent on the total pressure  $P$  (Norooz Oliaee et al. 2022; Rothman et al. 1998).

During the model fit, the horizontal scale  $t_i$  is mapped to wavenumber (in  $\text{cm}^{-1}$ ) of the gas absorption lines by a quadratic fit (Norooz Oliaee et al. 2022),

$$v_i = a_4 + a_5 t_i + a_6 t_i^2, \quad (6)$$

where  $a_4$ ,  $a_5$ , and  $a_6$  are fit parameters dependent on the rate of change of current sent to the laser. While it is also possible to calibrate wavenumber by comparing neighboring peaks, this approach calibrates at all  $i$  and allows for a more precise calibration.

Thus, TDLAS can provide a calibration-free determination of the  $\beta_{\text{abn}}$  of a gas, such as oxygen, relying only on absolute measurements of the gas molecular properties (as published in HITRAN), the sample cell length, and the temperature and pressure within the instrument.

### 2.3. Theory of photothermal spectroscopy and photothermal interferometry

Photothermal spectroscopy (PTS) refers to a collection of techniques by which sample heating by a light source (often modulated) is measured. PTS is distinct from photoacoustic spectroscopy (PAS), which measures acoustic waves generated by a light source and propagated away from the sample toward a detector. It is worth noting, however, that PTS is sometimes labeled as PAS due to the historical popularity of the latter (e.g., Krzempek et al. 2018). Nevertheless, PTS, and specifically its realization *via* PTI, has recently seen renewed interest for gas and aerosol characterization (Bialkowski, Astrath, and Proskurnin 2019; Davis

and Petuchowski 1981; Drinovec et al. 2022; Li, Wang, and Li 2016; Li et al. 2017; Lin and Campillo 1985; Radeschnig, Bergmann, and Lang 2024; Sedlacek 2006; Visser et al. 2020).

In PTI, a light source (such as a laser) first pumps energy into a system, resulting in local sample heating. This heating causes a temperature and therefore refractive-index change, described by the Clausius–Mossotti equation (Radeschnig, Bergmann, and Lang 2024):

$$\Delta n = \left( \frac{dn}{dT} \right) \Delta T \approx - \frac{(n_0 - 1)}{T_0} \Delta T, \quad (7)$$

where  $n$  and  $T$  are respectively the refractive index and temperature of the gas, and the subscript 0 indicates the reference temperature state. The light source is normally modulated, such that Equation (7) applies to each heating/cooling cycle in the instrument (Bialkowski, Astrath, and Proskurnin 2019), allowing for improved signal-to-noise. Of course, for particles, Equation (7) only holds when the sample is given adequate time to thermalize, which requires that  $\Delta n$  is measured on a timescale slower than the timescales required for relaxation (Gillis, Havey, and Hodges 2010) and transfer of energy from any absorbing aerosol particles to the gas. This is discussed further in Section 3.4.

When considering the phase shift  $\Delta\phi$  of an interferometer (e.g., a Mach-Zehnder or Jamin configuration), the change in refractive index given in Equation (7) depends on the interferometer wavelength  $\lambda_0$ , as well as the excitation-laser properties. If an excitation-laser with power  $P_e$  and beam radius  $a_e$  is modulated at frequency  $f_e$ , then the phase change can be stated as (Sedlacek 2006)

$$\Delta\phi = \frac{l_e}{2\lambda_0 a_e^2 \rho C_p} \cdot \frac{(n_0 - 1)}{T_0} \cdot \frac{\beta_{\text{abn}} \cdot P_e}{f_e}, \quad (8)$$

where  $\beta_{\text{abn}}$  is the combined absorption coefficient of the sample (gases and particles);  $\rho = p/RT$  is the density of air ( $1.20 \text{ kg m}^{-3}$ ) according to the pressure  $p$  and temperature  $T$  in the sample cell; and  $C_p$  is the specific heat of air ( $1005 \text{ J kg}^{-1} \text{ K}^{-1}$ ). The expected phase shifts are small,  $< 1 \text{ } \mu\text{rad}$  (Sedlacek 2006). Note that the path length  $l_e$  is the distance over which the excitation and interferometer beams overlap, and is a segment of the TDLAS path length  $l_g$ . We discuss the determination of  $l_g$  and  $l_e$  below.

## 2.4. Cross-calibration of PTI with reference-gas TDLAS

In order to calibrate PTI using reference TDLAS measurements of absorption ( $\beta_{\text{abn,ref}}$ ) from a known gas, we can rewrite Equation (8) as a simpler calibration equation. We first separate its parameters into those which are sample properties ( $\Delta\phi$ ,  $\beta_{\text{abn}}$ ,  $\rho$ ) and those which are not: instrument control parameters ( $P_e$ ,  $f_p$ ) kept constant between calibration and measurement, and physical constants or physical properties ( $\lambda_0$ ,  $a_p$ , ...). These non-sample properties can be grouped together using a calibration factor,

$$C_0 = \frac{l_e}{2\lambda_0 a_p^2 \rho C_p} \cdot \frac{(n-1)}{T_0} \cdot \frac{1}{f_e}, \quad (9)$$

such that,

$$\beta_{\text{abn}} = \frac{\Delta\phi}{C_0 P_e}. \quad (10)$$

We measured  $P_e$  using a photodetector, the calibration constant of which is implicitly incorporated into  $C_0$ . Thus, the PTI calibration factor  $C_0$  can be determined from the background-(bg) subtracted PTI phase shift caused by a known gas-absorption line as

$$C_0 = \left( \frac{\Delta\phi_{\text{gas}}}{P_{e,\text{gas}}} - \frac{\Delta\phi_{\text{bg}}}{P_{e,\text{bg}}} \right) \cdot \beta_{\text{abn,ref}}, \quad (11)$$

where  $\beta_{\text{abn,ref}}$  is known from TDLAS (at the same  $\lambda$ ) via Equation (2). Background subtraction is performed after power normalization, to account for potential changes in laser power between gas-absorption-line and background setpoints. Note that this calibration approach does not require any priori knowledge beyond the  $\beta_{\text{abn,ref}}$  obtained from TDLAS, and a measurement of the PTI background. The PTI background can be obtained either with  $N_2$ , or from a TL-PTI scan of HEPA-filtered air, the data from which can be fitted using Equation (3), as described for TDLAS above. Here, we performed of these methods and obtained identical results.

The particulate absorption coefficient  $\beta_{\text{abn,PM}}$  can then be calculated as

$$\beta_{\text{abn,PM}} = \beta_{\text{abn,total}} - \beta_{\text{HEPA}} \quad (12)$$

where  $\beta_{\text{abn,total}}$  is the total (background + PM) signal, and  $\beta_{\text{HEPA}}$  is the background signal observed for HEPA-filtered air due to potential background absorption (including window contamination) and noise sources.

## 2.5. TL-PTI prototype

Figure 1 shows a prototype which realizes the reference-gas cross-calibration concept presented here by combining TDLAS and PTI measurements. This prototype was used to generate all presented data. The interferometer is a folded Jamin interferometer (Moosmüller and Arnott 1996) similar to that used by Sedlacek (2006) for PTI. A pressure cell was used for maintaining quadrature.

The interferometer probe laser used here was a 632.8 nm frequency-stabilized HeNe (Thorlabs HRS015B). The entire setup shown in Figure 1 was enclosed in a simple acrylic box, and the HeNe laser tube was surrounded by additional insulating foam to minimize its temperature sensitivity. The probe laser was split by a 50.8 mm  $\varnothing$  window (Thorlabs WG42012; see Figure 1) treated in-house with custom partial-reflectivity, high-reflectivity, and anti-reflectivity coatings to act as a combined 50/50-beamsplitter-mirror in the folded Jamin interferometer. The geometrical arrangement of the custom coatings on the window (depicted in Figure 1) followed that originally demonstrated by Moosmüller and Arnott (1996). The coatings were fabricated in a Spector (Veeco, NY, USA) dual-ion-beam sputtering system, with SiO<sub>2</sub> and TiO<sub>2</sub> as the layer materials, using an automated deposition approach developed at NRC (Sullivan and Dobrowolski 1992). After alignment, the pressure-cell setpoint required to reach quadrature was determined by modulating the pressure in the pressure cell. The outputs of the interferometer were monitored by two Thorlabs PDA10A2 photodetectors with 632.8 nm filters (Thorlabs FLH633-1) and sent to a lock-in amplifier (SR830, Stanford Research Systems, USA), along with the reference signal generated by a function generator (Tektronix AFG3022B).

A dichroic mirror (Thorlabs DMSP650; see Figure 1) immediately following the beamsplitter acted as both the window to the measurement cell, and the means by which the probe and excitation lasers were combined, similarly to Davis and Petuchowski (1981). A second identical dichroic mirror was placed at the other end of the sample cell to separate the beams. The excitation laser was a so-called “mode-hop-free” TDL lasing at about 760 nm (Photodigm Inc., TX, USA, Model 760DBRH-MHFL) with 500 kHz linewidth and about 1 mm  $1/e^2$  beam diameter. The TDL was controlled by a benchtop laser temperature and current controller (LDC501, Stanford Research Systems). The output of the TDL was directed through an acousto-optical modulator (AOM; IntraAction USA, Parts AOM-402AF3 and ME-403-24),

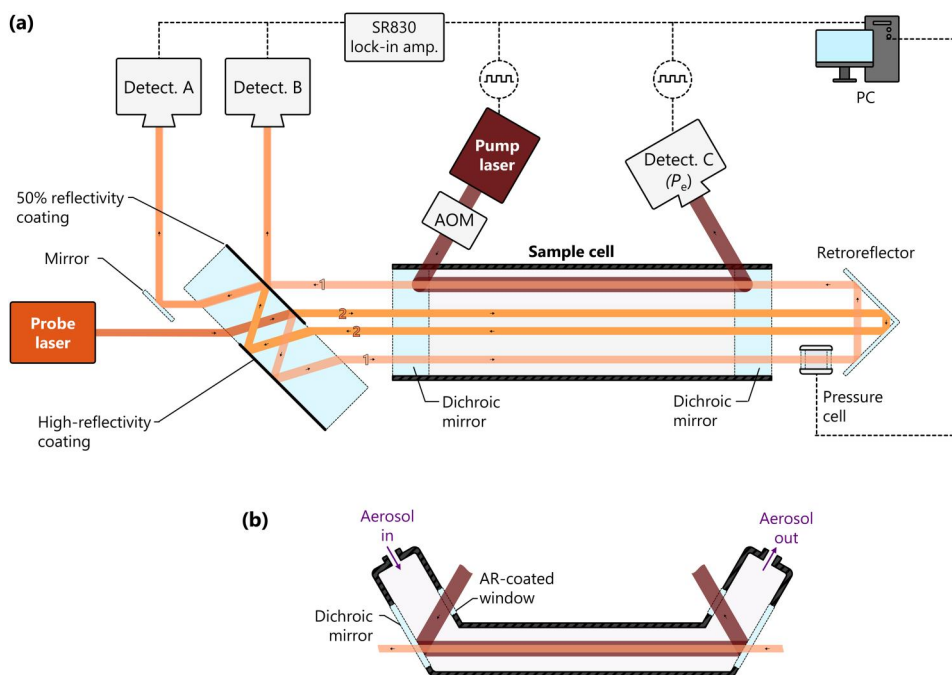


**Figure 1.** Schematic diagram of the tunable-laser PTI prototype. Orange lines indicate the probe laser (here, 632.8 nm), dark-red lines indicate the excitation laser (here, 760 nm). Detectors A and B monitor the interferometer while Detector C monitors the excitation laser power; all are photodiodes. AOM: acousto-optic modulator, PC: data acquisition system and personal computer. (a) emphasizes the optical paths, while (b) shows the aerosol flow path and the anti-reflectively (AR) coated windows through which the excitation laser enters and exits the sample cell. Dividing walls were present between the interferometer arms in the sample cell, but were not used in this study and are omitted for simplicity.

which served as a vibration-free method to TTL modulate the power sent to the sample cell. Due to the AOM, and to the fact that we did not operate the TDL at peak power, the actual power entering the cell at the peak  $O_2$  absorption line used for the measurements below was 60 mW. We found that direct square-wave modulation of the TDL current led to wavelength instabilities which manifested as artifacts in the gas absorption spectra discussed below, presumably because of the physical response of the TDL to its drive current. That is, by using an AOM for rapid modulation while a stable current was sent to the TDL, we allowed the TDL to stabilize in its wavelength output. The relative TDL power was monitored after exiting the cell by a large-area Thorlabs PDA100A2 detector (“Det C.” in Figure 1) to normalize for power variations during both TDLAS and TLPTI measurements. This power meter was calibrated by reference to a Gentec XLP12-3S-H2-D0 power meter. The TDL produced about 80 mW of power at its maximum.

Aerosols were pulled through this sample cell using a  $0.5 \text{ L min}^{-1}$  flow controlled by a critical orifice and pump. At this flow rate, no additional noise was observed at our 90 Hz measurement frequency in our prototype. The relationship between sample

flow and noise is expected to depend on parameters like sample-cell cross-section and choice of pump, and may be minimized by using Helmholtz resonators (Moosmüller, Chakrabarty, and Arnott 2009) in the future.

## 2.6. Nigrosin experiments

Experiments were conducted with a nigrosine solution ( $\approx 2 \text{ g/L}$ ; Sigma-Aldrich 198285, Lot # SHBL0637) in deionized water ( $>15 \text{ M}\Omega$ ). The solution was nebulized and dried with a diffusion drier (Topas ATM 226) before being diluted with a dilution bridge (as recommended in ISO 27891 Annex H). The dilution ratio (and thus concentration) was varied nonlinearly, to verify that long-term drift did not occur in the system. Then, excess flow was vented and the remainder was split between the NRC PTI and a scanning mobility particle sizer (SMPS; Model 3082 + 3776; TSI Inc., MN, USA). The SMPS measures the number distribution as a function of log-binned mobility diameter  $d_m$ ,  $dN/d\log d_m$ . The SMPS measurements were corrected for multiple charging and diffusion losses according to the manufacturer’s software (TSI AIM, version 11.4); polydisperse particles were measured by the PTI.

Because the volume-weighted SMPS size distributions extended above the maximum size measured by the SMPS (760 nm), we fitted lognormal curves to the SMPS data to obtain truncation-corrected volume distributions. This correction was relatively small, resulting in an additional 2–6% of  $\beta_{\text{abn}}$  as modeled by Mie calculations, as shown below. Two different Mie codes were used for cross-validation; PyMieScatt version 1.8 and the code of Peña and Pal (Peña and Pal 2009; Taylor et al. 2015).

The SMPS-measured volume distributions, measured at a range of dilution ratios, were used to fit the imaginary refractive index of nigrosine, with the real refractive index constrained to a value measured by spectroscopic ellipsometry (VASE, J.A. Woollam Co.) and spectrophotometry (Lambda-900, Perkin-Elmer, equipped with an integrating sphere, Labsphere), with both measurements performed on dried nigrosine films on N-BK7 glass substrates. The fitted refractive index was then used to predict  $\beta_{\text{abn}}$  from the SMPS measurements, for visualization of the results in terms of both size-resolved  $\beta_{\text{abn}}$ -weighted distributions  $d\beta_{\text{abn}}/d\log d_m$  and the overall integrated absorption coefficient  $\beta_{\text{abn}}$ . Uncertainty in this  $\beta_{\text{abn}}$  was expanded by 10% to account for inaccuracy in the SMPS-measured volume, which was estimated from the SMPS-mass-concentration uncertainty of >15% reported by previous studies (Liu et al. 2012; Momenimovahed and Olfert 2015). The TL-PTI uncertainty was also propagated from the standard error of the mean measured value, and expanded by a further 2% to represent observed variability in the calibration constant for our laboratory prototype.

### 3. Results and discussion

#### 3.1. Relative path lengths in TDLAS and PTI measurements

We determined the path length  $l_g$  by comparing the overall  $\text{O}_2$  TDLAS signals for our standard setup and for a dedicated experiment where the sample cell was filled with nitrogen. For the nitrogen experiment, the  $\text{O}_2$  optical depth changed by a factor  $0.796 \pm 0.011$  (this uncertainty was propagated from the fit coefficients). The path length within the PTI cell (which is shown in Figure 1 as a broad U-shape and includes two reflections off the dichroic mirrors) is  $281.24 \pm 0.13$  mm, with its uncertainty known from standard machining tolerances. Combining these values yields a total TDLAS path length of  $1378 \pm 18$  mm. (In our prototype, the TDL path length outside of the sample cell was considerably longer than the path

length within, in order to allow the incident and diffracted light exiting the AOM to separate in space.) Our relative calculation of the TDLAS path length avoids uncertainties in path length due to the various air gaps between the TDL and the PD shown in Figure 1. Moreover, this means that the path lengths in both TDL and PTI measurements are referenced to the same quantity.

#### 3.2. Calibration-free measurement of $\beta_{\text{abn}}$ of $\text{O}_2$ via TDLAS

Figure 2 shows the photodetector (PD) signal obtained when scanning the excitation laser wavelength across an oxygen line at 760 nm (upper red curve). The presented data represent one 10-s scan, and a corresponding fit to Equation (3). The fitted quadratic term was small (Table 1), indicating that the chosen Lorentzian absorption line shape and a mostly linear baseline model adequately describes the observed oxygen absorption feature and the relationship of power with current for the excitation laser. The approximate wavelength of these absorption lines was determined by scanning the laser across a much broader wavelength range (not shown) and comparing the result with HITRAN; the precise wavelength was determined by the fit. The oxygen concentration retrieved from the fit was  $20.27 \pm 0.07\%$  mol  $\text{O}_2$ /mol air. The results of the fit to Equation (3) are summarized in Table 1.

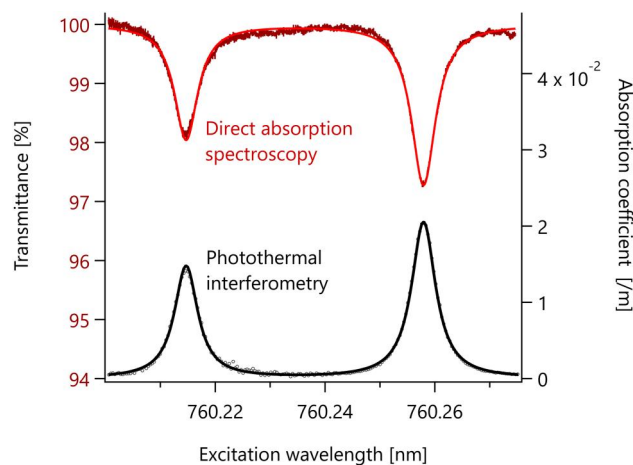


**Figure 2.** Measurement of two exemplary oxygen absorption lines at 760.215 and 760.258 nm by direct absorption spectroscopy (TDLAS) and by tunable-laser photothermal interferometry (TL-PTI). The upper curve shows the TDLAS transmittance spectrum obtained at the Detector C. The lower curve shows the PTI phase shift measured by the interferometer, *via* the lock-in amplifier. Curves and baselines (already subtracted) were obtained by fits to Equation (3).

**Table 1.** Results of the TDLAS fit to the oxygen absorption line *via* Equation (3).

Parameter	Best-fit value	Confidence interval (95%) <sup>#</sup>	Unit*	Description
$a_1$	3.80690	3.80670, 3.80711	V	Baseline offset term
$a_2$	9.1494	9.1445, 9.1543	$\times 10^{-4}$ V/d	Baseline slope term
$a_3$	-9.269	-9.446, -9.092	$\times 10^{-9}$ V/d <sup>2</sup>	Baseline quadratic term
$a_4$	13153.8990	13153.8960, 13153.9020	cm <sup>-1</sup>	High frequency end of data
$a_5$	-2.95	-2.97, -2.93	$\times 10^{-4}$ cm <sup>-1</sup> /d	Laser linear tuning rate
$a_6$	1.09	1.00, 1.17	$\times 10^{-9}$ cm <sup>-1</sup> /d	Laser non-linear tuning rate
[O <sub>2</sub> ]	0.2027	0.2020, 0.2034	atm.	Oxygen partial pressure
$V_0$	0.015	0.002	V	Detector zero level voltage <sup>†</sup>
$T$	296	2	K	Temperature <sup>†</sup>
$P$	1	0.02	atm	Ambient pressure <sup>†</sup>
$l_g$	1378	18	mm	TDLAS path length <sup>‡</sup>
$l_e$	281.24	0.13	mm	PTI path length <sup>x</sup>
$\chi^2$	$5.56 \times 10^{-3}$	n.a.	V <sup>2</sup>	Fit residual (SSE)

\* $d$  is 1/(DAQ Sampling rate) in units of (1e-5s).

<sup>†</sup>Fixed at measured values.

<sup>‡</sup>Fixed at the value obtained by relative path-length measurements (see Section 2.2).

<sup>#</sup>From fit, or from repeated measurements.

<sup>x</sup>Measured value, used when predicting PTI signals from Equation (3) independently of the oxygen fit.

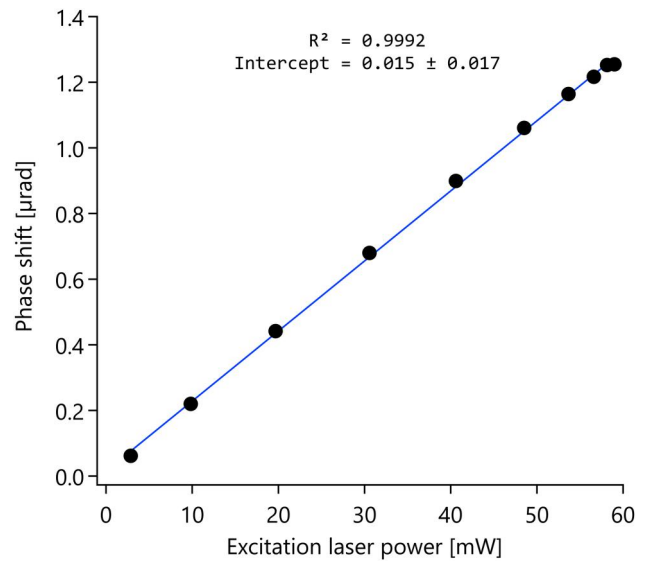
### 3.3. TL-PTI measurement of $\beta_{abn}$ of O<sub>2</sub>

Figure 2 also shows the PTI signal obtained during a slow TDL wavelength scan where 243 points were measured during 15 min. (TDLAS data obtained simultaneously with this 15-min scan were comparable to the TDLAS data obtained from a 10-second scan.) The background-subtracted PTI data display the same O<sub>2</sub> absorption lines as the TDLAS data, and can thus be cross-calibrated.

The TL-PTI data shown in Figure 2 reflect HEPA-filtered ambient air, with background signals determined in the same way as for TDLAS, by fitting Equation (3). Thus, the two curves quantify the same absorption lines of oxygen. During routine TL-PTI measurements, a much faster scan can be performed with these same parameters (e.g., 30 s) by reducing the range of  $\lambda$  scanned to focus on a known absorption line, allowing rapid checks to be interspersed between more careful 15-min calibrations.

While it would be possible to obtain TDLAS and PTI peak scans for O<sub>2</sub> even in the presence of particles in the cell, the PTI scan needs to be relatively slow to allow for steady-state temperatures to be reached in the cell. Steady-state temperatures change as a function of  $P_e$  and  $\beta_{abn}$  because the instrument heating cycle is too fast to allow for complete cooling between laser-on periods (Bialkowski, Astrath, and Proskurnin 2019). Thus, PTI wavelength scans are expected to be slower than variations in the aerosol loading and to lead to distortion of the measured peaks. We therefore recommend that absolute TDLAS calibration be performed as part of routine, automated HEPA-filter measurements, e.g., every 10 min.

We performed an additional experiment to verify that our fitted PTI background signals represented the true background, by filling the sample cell with



**Figure 3.** Linearity of the calibrated TL-PTI signal  $\beta_{abn}$  with TDL excitation laser power  $P_e$  at the 760.258 nm O<sub>2</sub> absorption line. The  $P_e$  was controlled by varying the diffraction efficiency of the AOM, which varied the fraction of transmitted laser power, while modulating at 90 Hz. This allowed the remainder of the system to be operated at constant conditions. The phase shift  $\Delta\phi$  corresponds to a  $\beta_{abn}$  of  $0.02\text{ m}^{-1}$  and the laser power reported on the abscissa.

nitrogen and repeating the experiment shown in Figure 2. The results showed a similar background as our fit to Equation (3), verifying the interpretation given above. Since the PTI background can be fitted, nitrogen is not needed for routine instrument operation.

We also performed an additional experiment to demonstrate the linear relationship  $\beta_{abn} \propto \Delta\phi/C_0P_e$  given in Equation (10). Figure 3 shows that varying the laser power  $P_e$  results in a linear change in absorption coefficient  $\beta_{abn}$ , as calculated from the measured interferometer phase shift  $\Delta\phi$ . Thus, our

use of a calibration constant (rather than calibration function) is justified. We note that the consistency between the Lorentzian absorption lines measured by TDLAS and by PTI in Figure 2 also demonstrated the linearity of our PTI system.

Finally, we also note that the measurements in Figure 2 and Figure 3 all represent the mean of several seconds of measurements, recorded a few seconds after the excitation laser was switched on. Thus, the observed linearity in  $\beta_{\text{abn}}$  with different  $P_e$  indicates no relationship between the absolute temperature change of our sample and the measured  $\beta_{\text{abn}}$ . This absolute temperature change was calculated as 1.2 mK per cycle for our system at 80 mW (Equation 9 of Mazzoni and Davis 1991) when targeting the  $\beta_{\text{abn}}$  of  $\text{O}_2$ . However, since the sample volume does not cool completely between periods, the actual peak temperature may be larger by a factor of  $\approx 2$  after tens of heating cycles (Bialkowski, Astrath, and Proskurnin 2019), which is still  $\ll 1$  K.

This temperature change is minor, and far below the change required to appreciably affect the measured Lorentzian lineshapes measured by TDLAS and PTI. To illustrate this further, we calculated the change in lineshapes expected for a temperature change of 20 K (which might occur when sampling from combustion sources) using Equation (3) and Table 1, and found that the resulting curve was visually indistinguishable from the unheated case. Frequent calibrations should nevertheless be employed to monitor for any issues.

### 3.4. Timescales for PTI modulation

While the modulation frequency,  $f_e$ , is generally flexible, it is subject to certain practical constraints due to the timescales of underlying physical processes. First, both signals and noise in a PTI instrument generally increase at lower frequencies, although at different rates. The difference between these inverse-frequency relationships results in a minimum  $f_e$  below which noise increases faster than signal.

At the other extreme, it is important that  $f_e$  be kept small so that the PTI system gives sufficient time for excitation-laser energy to be thermalized. This requirement is not independent of the first constraint, since greater thermalization results in greater signal. However, it is essential to acknowledge that there are other physical limits to the system, especially when calibrating the PTI signal with gas absorption lines.

For the oxygen reference gas chosen here, the initial excitation of an absorption line results in an

excited-state  $\text{O}_2$  which most efficiently decays by collisional relaxation with  $\text{H}_2\text{O}$  (Gillis, Havey, and Hodges 2010). Since  $\text{H}_2\text{O}$  concentrations vary broadly between dry and wet air, this may lead to an undesired and large sensitivity of the PTI response to  $\text{O}_2$  with variations in relative humidity. For example, in their PAS system modulated at 1.6 kHz, Gillis, Havey, and Hodges (2010) observed an  $\approx 8$ -fold change in sensitivity of their PAS system between low- $\text{H}_2\text{O}$  and high- $\text{H}_2\text{O}$  samples (ranging from 1% to 90% relative humidity at 20 °C). This sensitivity must be avoided when  $\text{O}_2$  is used for PTI calibration, as discussed in this subsection.

Figure 4 shows the timescales of  $\text{O}_2$  relaxation, just discussed, as well as that of PTI and PAS sensitivity and PAS sensitivity. Also included is the timescale of thermal diffusion from the center to the edge of the excitation-laser beam (Radeschnig, Bergmann, and Lang 2024), which represents an upper limit for any modulated PTI instrument. Broadband acoustic noise is generally also important, but is not shown in Figure 4 due its broadband nature. The variability in  $\text{O}_2$  relaxation timescale due to variation in  $\text{H}_2\text{O}$  concentration is shown by the broad black line (representing the broad range of  $\text{H}_2\text{O}$  concentrations explored by Gillis, Havey, and Hodges 2010). The range of values shown for other properties represent the physical parameters of devices reported in the literature or herein. Details of these calculations are given in Table 2.

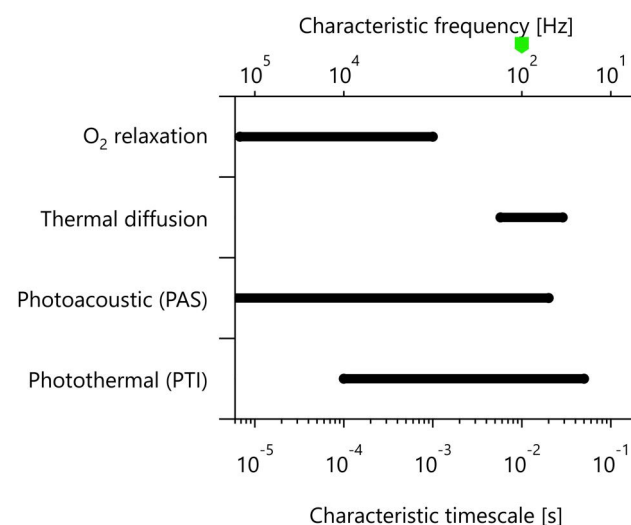


**Figure 4.** Key timescales involved in PTI, calculated from the values in Table 2. The green arrow at top indicates our measurement  $f_e$ , where enough time has been given for  $\text{O}_2$  relaxation (a bottleneck in signal generation) but where acoustic noise (not shown) is minimized relative to even lower frequencies. This region is not accessible for PAS resonators designed for high frequencies ( $f_p > 1$  kHz).

**Table 2.** Key timescales involved in PTI, as illustrated in Figure 4.

Phenomenon	$\tau$ lower [s]	$\tau$ upper [s]	Note	Reference
Photothermal (PTI, PAS, ...)	$5 \times 10^{-3}$	$5 \times 10^{-2}$	Decreases with $f_e$	PTI: raw data; PAS: Yang, Chen, and Wang (2021), Karhu et al. (2022)
Acoustic noise	$\ll 1/f_e$	$> 0.1$	Decreases with $f_e$	Raw data
Thermal diffusion	0.023	0.115	Radial only (axial much slower)	Radeschnig, Bergmann, and Lang (2024), with $a_0 = 3$ mm and $\sigma_p = 1$ mm
O <sub>2</sub> relaxation	$6.8 \times 10^{-6}$	$1 \times 10^{-3}$	Timescale range represents the influence of H <sub>2</sub> O	Gillis, Havey, and Hodges (2010)

The figure shows that the excitation-laser-modulation timescale of our NRC PTI prototype (highlighted by the green arrow) is much greater than the timescale of even the slowest O<sub>2</sub> relaxation rate, such that our prototype will be insensitive to the H<sub>2</sub>O concentration. This result is also applicable to any PTI or PAS system (Drinovec et al. 2022; Karhu et al. 2022; Lee and Kim 2012; Radeschnig et al. 2021; Sedlacek 2006; Visser et al. 2020) which operates at a similar order-of-magnitude in  $f_e$ .

We also experimentally validated these conclusions by measuring the PTI signal for O<sub>2</sub> at  $f_e = 100$  Hz, at 7 different relative humidities, ranging from 10% to 90%. Each measurement was not statistically different from the others, demonstrating an insensitivity to H<sub>2</sub>O concentrations. Baseline signals (where  $\lambda$  was chosen such that  $\beta_{\text{abn}, \text{O}_2} \rightarrow 0$ ) were also insensitive to variations in [H<sub>2</sub>O].

### 3.5. Imaginary refractive index retrieval

As a demonstration of our system, Figure 5 shows a comparison between our self-calibrated TL-PTI measurements and the  $\beta_{\text{abn}}$  calculated for nebulized nigrosine nanoparticles based on their size distribution and fitted  $k = 0.168 \pm 0.005$ . For this fit, we constrained  $n$  to the value of  $1.790 \pm 0.008$  found from analysis of spectroscopic ellipsometry and diffuse transmittance data.

The spectroscopic ellipsometry and diffuse transmittance analysis gave  $k$  values of 0.16–0.19 (range of repeated measurements), which encompasses the more precise value obtained from repeated TL-PTI and SMPS measurements. The poor repeatability of these  $k$  values is attributed to a greater dependence on the film-thickness variability, reflection from the back of the sample (the film was semi-transparent at 760 nm) and the scattering (surface and bulk) of the nigrosine-on-glass film (Joerger et al. 1997).

Our fitted  $k$  is not significantly different from the  $k = 0.1601 \pm 0.0066$  measured by Bluvshstein et al. (2017) using spectroscopic ellipsometry of a nigrosine film. It is somewhat larger than the value of Drinovec et al. (2022), who reported  $k = 0.142$  for a nigrosine

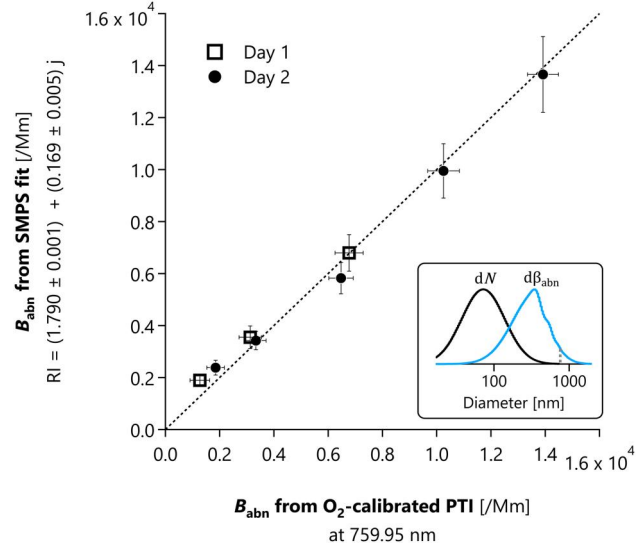


**Figure 5.** Scatterplot of  $\beta_{\text{abn}}$  calculated for nebulized nigrosine nanoparticles based on their size distribution (SMPS) and refractive index (real refractive index  $n$  measured by ellipsometry, imaginary refractive index  $k = 0.168 \pm 0.005$  determined from self-calibrated TL-PTI), plotted against self-calibrated TL-PTI measurements of  $\beta_{\text{abn}}$ . The TL-PTI  $k$  was determined by fitting the TL-PTI data as reference to the SMPS-measured nigrosine volume. The inset shows the number- and absorption-weighted SMPS distributions,  $dN/d\log d_m$  and  $d\beta_{\text{abn}}/d\log d_m$ . The vertical dashed grey line shows the point above which the SMPS data were extrapolated by lognormal fitting. Error bars represent the propagated uncertainties discussed in the text. The deviation of the PTI signal at lower  $\beta_{\text{abn}}$  is mostly attributed to noise in our prototype interferometer.

film, based on Brewster angle measurements. While our value is in excellent agreement with that of Bluvshstein et al. (2017), the discrepancy with that of Drinovec et al. (2022) suggests variability in the properties of nigrosine between batches, as also hypothesized by Drinovec et al. (2022). The fact that our aerosol-phase measurements agree with the film measurements of Bluvshstein et al. (2017) suggest that the phase of the material is unimportant to the measured value of  $k$ , as expected. However, our approach avoids both the additional effort and the additional uncertainty involved in relying on film-based refractive index measurements of a non-standardized material such as nigrosine.

## 4. Literature context

### 4.1. Comparison with other approaches to calibrating aerosol absorption

A few related approaches to cross-calibrating aerosol absorption with gases have been previously reported in the context of both PAS and PTI.

In PTI, as well as PAS, calibration has often been achieved with broadband light absorbing gases such as ozone (Lack et al. 2006) or nitrogen dioxide ( $\text{NO}_2$ ) at 532 nm wavelength (Arnott, Moosmüller, and Walker 2000; Drinovec et al. 2022; Sedlacek 2006). Lack et al. (2006) determined their reference ozone concentrations using 532 nm cavity ring-down spectroscopy and suggested that commercial ozone monitors could also be used as references, although later work showed that ozone photodissociation was a source of substantial error (Fischer and Smith 2018). Drinovec et al. (2022) determined their reference  $\text{NO}_2$  concentrations using a portable, traceably calibrated  $\text{NO}_2$  monitor.

The use of an independent reference measurement introduces uncertainties due to sample transport, particularly for the chemically labile  $\text{NO}_2$ . Also,  $\text{NO}_2$  cannot easily be quantified *via* its absorption lines at the blue/green wavelengths of interest in atmospheric science (though it can be used to infer  $\beta_{\text{ext}}$ , as discussed above). Moreover, our oxygen-based approach is advantageous over  $\text{NO}_2$  and  $\text{O}_3$  due to oxygen's ubiquitous presence in ambient air at high concentrations.

Alternatively, Arnott, Moosmüller, and Walker (2000) showed that PAS instruments can be cross-calibrated without the use of an external reference device, using extinction measurements of high concentrations of an absorbing gas like  $\text{NO}_2$  in the PAS cell, although external (independent) calibrations of the PAS microphone and photodetector were needed. They used a 532 nm laser and about 500 ppm of  $\text{NO}_2$ . Using an internal piezoelectric disk to calibrate the resonance frequency and quality factor of their acoustic resonator, they calculated a  $\beta_{\text{abn},532\text{nm}}$  from 500 Hz PAS signals ( $0.16 \text{ m}^{-1}$ ) that agreed well with extinction measurements. Thus, Arnott, Moosmüller, and Walker (2000) demonstrated that PAS can be calibrated from  $\beta_{\text{ext}}$ . Al Fischer and Smith (2018) also calibrated their system using  $\beta_{\text{ext}}$  of  $\text{NO}_2$ , but used a cavity ring-down spectrometer in series with their photoacoustic cell, in order to also measure  $\beta_{\text{ext,PM}}$  routinely. Our system differs from these measurements of  $\beta_{\text{ext}}$  in that we exploit a tunable laser to identify oxygen absorption lines (as well as instrument background) unambiguously, and do not require an external calibration sample. Also, as we employ TDLAS, no photodetector

calibration is necessary, and orders-of-magnitude lower gas-absorption signals can be used. Lower calibration reference signals can be obtained by reducing the laser power with an AOM (as done here), by using optical filters, or by selecting a weaker absorption line. The precise lower limit will depend on instrument signal-to-noise, which has not been optimized in our current prototype. Finally, as our system utilizes PTI rather than PAS, there is no microphone calibration required.

Later work by the same team (Tian, Moosmüller and Arnott 2009) showed that simultaneous wavelength-modulation spectroscopy (WMS) could be accomplished within a PAS cell, rather than extinction calculations. Tian, Moosmüller and Arnott (2009) utilized a 760-to-770 nm external-cavity laser, and thus measured oxygen A-band absorption, which inspired our approach. They performed PAS measurements at 1.5 kHz and WMS measurements at 10 Hz. It is worth noting that the laser used here takes advantage of a recently available, more compact and lower-cost technology than that used by Tian et al. More importantly, the use of PAS and WMS at different operating frequencies leads to a major uncertainty due to the slow relaxation timescale of  $\text{O}_2$ , as shown later by Gillis, Havey, and Hodges (2010). In particular, as relative humidity varies, the resulting PAS efficiency may vary by almost one order of magnitude. We have avoided this issue in our PTI approach because of the slow 90 Hz power modulation in our instrument, as discussed above. In addition, Tian, Moosmüller and Arnott (2009) did not measure oxygen concentrations directly, as done here using TLDAS, but rather employed a reference value of 20.95%.

The extinction method reported by Arnott, Moosmüller, and Walker (2000) is similar to the calibration method used in a commercial device, the photoacoustic extinctions (PAX) produced by Droplet Measurement Technologies (DMT Inc., CO, USA). In that device, high concentrations of PM are used to calibrate first a nephelometer (measuring light scattering integrated from  $6^\circ$  to  $174^\circ$  [Beuttell and Brewer 1949; Marcos A. Peñaloza 1999]) using non-absorbing particles, then a PAS cell (using  $a \approx 1 \text{ W}$ , 870 nm laser) using light-absorbing particles. The nephelometer calibration is necessary in order to translate the  $\beta_{\text{ext}}$  obtained from a photodetector into  $\beta_{\text{abn}}$ , *via*  $\beta_{\text{abn}} = \beta_{\text{ext}} - \beta_{\text{sca}}$ . The resulting calibration has been shown to extrapolate linearly down from the high PM concentrations required for calibration (about  $20,000 \text{ Mm}^{-1}$ ) to the atmospherically relevant concentrations normally measured (about  $100 \text{ Mm}^{-1}$ ) (Corbin

et al. 2020), as has also been demonstrated for other PAS instruments (Arnott, Moosmüller, and Walker 2000; Lack et al. 2006). However, the use of high PM concentrations for calibration introduces a high risk of contaminating the instrument during the calibration procedure itself, which is avoided by our gas-based approach (though contamination during subsequent PM sampling may occur, and should be addressed by frequent calibration). In addition, this approach requires two different reference substances, whereas our approach can exploit ambient gases as ubiquitous internal standards for calibration. Nevertheless, the PAX approach has the benefit of being excitation-laser agnostic, as it exploits the broadband extinction properties of PM.

The extinction approach could also be used to calibrate a PTI instrument, with a non-tunable laser, by introducing a calibrant gas mixture with a large  $\beta_{\text{ext}}$  and comparing with a reference gas mixture with a negligible  $\beta_{\text{ext}}$ , at the wavelength of interest. If one of these gases was filtered air, this procedure would only require one reference substance. However, the procedure then requires a source of this reference gas, such as a compressed-air cylinder or a reaction-based generator. A major advantage of directly measuring a gas absorption line of ambient oxygen is that both the calibration signal and the interferometer background ( $\Delta\phi_{\text{bg}}$  in Equation (11), representing electronic noise, background vibrations, etc.) are measured at once, from the height and baseline of the peak.

Drinovec et al. (2022) also demonstrated the use of nigrosine as a transfer standard between absorbing gases and infrared wavelengths, where the wavelength-dependent complex refractive index of nigrosine is measured independently by ellipsometry. This is an approach that remains viable in an oxygen-calibrated PTI instrument such as ours. Alternatively, it is feasible to cross-calibrate lasers in our prototype by simple physical alignment, since our excitation laser is collimated and collinear with our interferometer laser. Then, the calibration factor  $C_0$  in Equations (10) and (11) would only need to be adjusted by the ratio of power  $P_e$  for the two lasers.

#### 4.2. Potential improvements

There are a number of simple extensions that can be made to our prototype. The system can be extended to include multiple lasers using standard dichroic mirrors prior to the excitation laser injection, combined with time- or frequency-multiplexing. Overlap of these beams with the calibration laser should be optimized

using, for example, optical apertures. Measurement of the beam profiles at the entry and exit of the sample cell can be used to quantify and constrain any uncertainty in beam collimation.

The prototype used here has not been optimized for signal-to-noise, which may be achieved through the use of a more stable interferometer laser; thermal and acoustic isolation of the measurement region; and improved data acquisition. Other improvements, such as switching valves (Karhu et al. 2022) or acoustic notch filters (also known as Helmholtz resonators) to acoustically isolate the sample region (Cotterell et al. 2019; Patrick Arnott et al. 1999) may further improve the signal-to-noise.

For applications where the reference gas concentration may differ between the sample cell and its surroundings, uncertainty in the TDLAS calibration may be reduced by enclosing the sample cell surroundings in a vacuum-pumped chamber. Conversely, a valve may simply be switched so that the sample pumped into the cell is drawn from the cell surroundings, ensuring reference-gas homogeneity. Alternatively, a gas specially introduced into the sample stream may be used.

For reference gases present at low concentrations, where a higher sensitivity may be desired than that provided by TDLAS, calibration-free wavelength-modulation spectroscopy, which may enhance signal-to-noise ratios by factors around 4 (Rieker, Jeffries, and Hanson 2009) may be employed.

## 5. Conclusions

We have presented and demonstrated an aerosol PTI instrument in which  $\beta_{\text{abn}}$  calibration is achieved by quantifying the absorption line(s) of a reference gas *via* TDLAS, without any external reference measurements. In the case of this work oxygen gas present in the ambient air was used for calibration. Oxygen is convenient for its atmospheric ubiquity, its absorption in the near-infrared (a region of interest for nanoparticles such as soot), and its chemical inertness relative to  $\text{NO}_2$  or  $\text{H}_2\text{O}$ . However, if desired, our method is applicable to any other calibration gases with resolvable absorption features.

The reference gas concentration is determined independently of the PTI system, using TDLAS, but with the same laser as is used to generate the PTI signal. Thus, our instrument is capable of self-calibrating as frequently as every minute, if required. Uncertainties due to laser alignment, sensitivity, and drift can therefore be minimized. Because our PTI system operates at

low frequencies ( $\sim 100$  Hz), sufficient time is given for the reference gas to fully thermalize, which is not the case for PAS performed at higher frequencies ( $> 1$  kHz) (Gillis, Havey, and Hodges 2010; Tian, Moosmüller and Arnott 2009). Our method can fulfill the requirements of a primary method of measurement in that all measurements are traceable to SI units, since the only non-relative measurements made are the path length of the PTI cell, ambient temperature, and ambient pressure. Future work will focus on the uncertainty in this method and on the cross-calibration of other lasers in multi-wavelength systems.

## Acknowledgements

CRedit: **Joel C. Corbin**: Conceptualization, Methodology, Formal analysis, Investigation, Writing – original draft preparation, Writing – review and editing, Visualization; **Alireza Moallemi**: Conceptualization, Methodology, Formal analysis and investigation, Writing – review and editing; **Daniel Poitras**: Design and fabrication of custom optical components, Ellipsometry, Formal analysis; **Timothy A. Sipkens**: Funding acquisition, Writing – review and editing, Visualization; **Jalal Norooz Oliiae**: Conceptualization, Methodology, Formal analysis, Investigation, Writing – review and editing, Funding acquisition.

The authors are grateful to Dr. Greg J. Smallwood and Dr. Rym Mehri for helpful discussions; to Chase Sun for assistance with sample-cell design; and to an anonymous reviewer for their helpful comments.

## Disclosure statement

No potential conflict of interest was reported by the author(s).

## Funding

This work was funded by the Government of Canada.

## ORCID

Joel C. Corbin  <http://orcid.org/0000-0002-2584-9137>  
 Alireza Moallemi  <http://orcid.org/0000-0002-9491-1993>  
 Daniel Poitras  <http://orcid.org/0000-0003-4403-8214>  
 Timothy A. Sipkens  <http://orcid.org/0000-0003-1719-7105>  
 Jalal Norooz Oliiae  <http://orcid.org/0000-0003-3839-2313>

## References

Al Fischer, D., and G. D. Smith. 2018. A portable, four-wavelength, single-cell photoacoustic spectrometer for ambient aerosol absorption. *Aerosol Sci. Technol.* 52 (4): 393–406. doi:10.1080/02786826.2017.1413231.

- Arnott, W. P., H. Moosmüller, and J. W. Walker. 2000. Nitrogen dioxide and kerosene-flame soot calibration of photoacoustic instruments for measurement of light absorption by aerosols. *Rev. Sci. Instrum.* 71 (12):4545–52. doi:10.1063/1.1322585.
- Beuttell, R. G., and A. W. Brewer. 1949. Instruments for the measurement of the visual range. *J. Sci. Instrum.* 26 (11): 357–9. doi:10.1088/0950-7671/26/11/302.
- Bialkowski, S. E., N. G. C. Astrath, and M. A. Proskurnin. 2019. Photothermal spectroscopy methods. In *Photothermal spectroscopy methods*, 1–56. Hoboken, NJ: John Wiley & Sons, Inc.
- Bluvshstein, N., P. Lin, J. M. Flores, L. Segev, Y. Mazar, E. Tas, G. Snider, C. Weagle, S. S. Brown, A. Laskin, et al. 2017. Broadband optical properties of biomass-burning aerosol and identification of brown carbon chromophores. *JGR. Atmospheres* 122 (10):5441–56. doi:10.1002/2016JD026230.
- Bohren, C. F. 1986. Applicability of effective-medium theories to problems of scattering and absorption by nonhomogeneous atmospheric particles, in. *J. Atmos. Sci.* 43 (5):468–75. doi:10.1175/1520-0469(1986)043<0468:AOEMTT>2.0.CO;2.
- Corbin, J. C., H. Czech, D. Massabò, F. B. de Mongeot, G. Jakobi, F. Liu, P. Lobo, C. Mennucci, A. A. Mensah, J. Orasche, et al. 2019. Infrared-absorbing carbonaceous tar can dominate light absorption by marine-engine exhaust. *Npj Clim. Atmos. Sci.* 2 (12) doi:10.1038/s41612-019-0069-5.
- Corbin, J. C., A. Moallemi, F. Liu, S. Gagné, J. S. Olfert, G. J. Smallwood, and P. Lobo. 2020. Closure between particulate matter concentrations measured ex situ by thermal-optical analysis and in situ by the cpm-electrometer reference mass system. *Aerosol Sci. Technol.* 54 (11):1293–309. doi:10.1080/02786826.2020.1788710.
- Cotterell, M. I., G. P. Ward, A. P. Hibbins, J. M. Haywood, A. Wilson, and J. M. Langridge. 2019. Optimizing the performance of aerosol photoacoustic cells using a finite element model. Part I: Method validation and application to single-resonator multipass cells. *Aerosol Sci. Technol.* 53 (10):1107–27. doi:10.1080/02786826.2019.1650161.
- Daun, K., J. Menser, R. Mansmann, S. T. Moghaddam, T. Dreier, and C. Schulz. 2017. Spectroscopic models for laser-heated silicon and copper nanoparticles. *J. Quant. Spectrosc. Radiat. Transfer* 197:3–11. doi:10.1016/j.jqsrt.2016.10.006.
- Davis, C. C., and S. J. Petuchowski. 1981. Phase fluctuation optical heterodyne spectroscopy of gases. *Appl. Opt.* 20 (14):2539–54. doi:10.1364/ao.20.002539.
- Drinovec, L., U. Jagodič, L. Pirker, M. Škarabot, M. Kurtjak, K. Vidović, L. Ferrero, B. Visser, J. Röhrbein, E. Weingartner, et al. 2022. A dual-wavelength photothermal aerosol absorption monitor: Design, calibration and performance. *Atmos. Meas. Tech.* 15 (12):3805–25. doi:10.5194/amt-15-3805-2022.
- Fischer, D. A., and G. D. Smith. 2018. Can ozone be used to calibrate aerosol photoacoustic spectrometers? *Atmos. Meas. Tech.* 11 (12):6419–27. doi:10.5194/amt-11-6419-2018.
- Gillis, K. A., D. K. Havey, and J. T. Hodges. 2010. Standard photoacoustic spectrometer: Model and validation using o 2 a -band spectra. *Review of Scientific Instruments* 81 (6):1–13. doi:10.1063/1.3436660.
- Gordon, I. E., L. S. Rothman, R. J. Hargreaves, R. Hashemi, E. V. Karlovets, F. M. Skinner, E. K. Conway, C. Hill, R. V.

- Kochanov, Y. Tan, et al. 2022. The HITRAN2020 molecular spectroscopic database. *J. Quant. Spectrosc. Radiat. Transfer* 277:107949. doi:10.1016/j.jqsrt.2021.107949.
- Haisch, C. 2012. Photoacoustic spectroscopy for analytical measurements. *Meas. Sci. Technol.* 23 (1):012001. doi:10.1088/0957-0233/23/1/012001.
- Hyvärinen, A.-P., V. Vakkari, L. Laakso, R. K. Hooda, V. P. Sharma, T. S. Panwar, J. P. Beukes, P. G. van Zyl, M. Josipovic, R. M. Garland, et al. 2013. Correction for a measurement artifact of the multi-angle absorption photometer (MAAP) at high black carbon mass concentration levels. *Atmos. Meas. Tech.* 6 (1):81–90. doi:10.5194/amt-6-81-2013.
- Joerger, R., K. Forcht, A. Gombert, M. Köhl, and W. Graf. 1997. Influence of incoherent superposition of light on ellipsometric coefficients. *Appl. Opt.* 36:319–27. doi:10.1364/ao.36.000319.
- Karhu, J., J. Kuula, A. Virkkula, H. Timonen, M. Vainio, and T. Hieta. 2022. Cantilever-enhanced photoacoustic measurement of light-absorbing aerosols. *Aerosol Sci. Technol.* 56 (1):92–100. doi:10.1080/02786826.2021.1998338.
- Koskinen, V., J. Fonsen, K. Roth, and J. Kauppinen. 2008. Progress in cantilever enhanced photoacoustic spectroscopy. *Vib. Spectrosc.* 48 (1):16–21. doi:10.1016/j.vibspec.2008.01.013.
- Krzempek, K., G. Dudzik, K. Abramski, G. Wysocki, P. Jaworski, and M. Nikodem. 2018. Heterodyne interferometric signal retrieval in photoacoustic spectroscopy. *Opt. Express.* 26 (2):1125–32. doi:10.1364/oe.26.001125.
- Lack, D. A., E. R. Lovejoy, T. Baynard, A. Pettersson, and A. R. Ravishankara. 2006. Aerosol absorption measurement using photoacoustic spectroscopy: Sensitivity, calibration, and uncertainty developments. *Aerosol Sci. Technol.* 40 (9):697–708. doi:10.1080/02786820600803917.
- Lack, D. A., H. Moosmüller, G. R. McMeeking, R. K. Chakrabarty, and D. Baumgardner. 2014. Characterizing elemental, equivalent black, and refractory black carbon aerosol particles: A review of techniques, their limitations and uncertainties. *Anal. Bioanal. Chem.* 406 (1):99–122. doi:10.1007/s00216-013-7402-3.
- Lee, J., and J. K. Kim. 2012. A measurement of light absorption using an image-based technique. *Exp. Therm. Fluid Sci.* 38:14–8. doi:10.1016/j.expthermflusc.2011.10.016.
- Lewis, K., W. P. Arnott, H. Moosmüller, and C. E. Wold. 2008. Strong spectral variation of biomass smoke light absorption and single scattering albedo observed with a novel dual-wavelength photoacoustic instrument. *J. Geophys. Res.* 113 (D16). doi:10.1029/2007JD009699.
- Li, B., Y. Wang, and Z. Li. 2016. A method for monitoring mass concentration of black carbon particulate matter using photothermal interferometry. *Environ. Sci. Pollut. Res. Int.* 23 (5):4692–9. doi:10.1007/s11356-015-5702-1.
- Li, Z., Z. Wang, F. Yang, W. Jin, and W. Ren. 2017. Mid-infrared fiber-optic photothermal interferometry. *Opt. Lett.* 42 (18):3718–21. doi:10.1364/ol.42.003718.
- Lin, H.-B., and A. J. Campillo. 1985. Photothermal aerosol absorption spectroscopy. *Appl. Opt.* 24 (3):422–33. doi:10.1364/ao.24.000422.
- Liu, Z., J. Swanson, D. B. Kittelson, and D. Y. H. Pui. 2012. Comparison of methods for online measurement of diesel particulate matter. *Environ. Sci. Technol.* 46 (11):6127–33. doi:10.1021/es3003537.
- Ma, Y. 2020. Recent advances in qepas and qepts based trace gas sensing: A review. *Front. Phys.* 8:545537. doi:10.3389/fphys.2020.00268.
- Marcos A. Peñaloza, M. 1999. Deriving the basic cell-reciprocal integrating nephelometer equation and its use for calibration purposes: A comprehensive approach. *Meas. Sci. Technol.* 10 (1):R1–R15. doi:10.1088/0957-0233/10/1/003.
- Mazzoni, D. L., and C. C. Davis. 1991. Trace detection of hydrazines by optical homodyne interferometry. *Appl. Opt.* 30 (7):756–64. doi:10.1364/ao.30.000756.
- Modini, R. L., J. C. Corbin, B. T. Brem, M. Irwin, M. Bertò, R. E. Pileci, P. Fetfatzis, K. Eleftheriadis, B. Henzing, M. M. Moerman, et al. 2021. Detailed characterization of the caps single-scattering albedo monitor (CAPS PM<sub>SSA</sub>) as a field-deployable instrument for measuring aerosol light absorption with the extinction-minus-scattering method. *Atmos. Meas. Tech.* 14 (2):819–51. doi:10.5194/amt-14-819-2021.
- Momenimovahed, A., and J. S. Olfert. 2015. Effective density and volatility of particles emitted from gasoline direct injection vehicles and implications for particle mass measurement. *Aerosol Sci. Technol.* 49 (11):1051–62. doi:10.1080/02786826.2015.1094181.
- Moosmüller, H., and W. P. Arnott. 1996. Folded jamin interferometer: A stable instrument for refractive-index measurements. *Opt. Lett.* 21 (6):438–40. doi:10.1364/ol.21.000438.
- Moosmüller, H., and W. P. Arnott. 2009. Particle optics in the rayleigh regime. *J. Air Waste Manag. Assoc.* 59 (9):1028–31. doi:10.3155/1047-3289.59.9.1028.
- Moosmüller, H., R. K. Chakrabarty, and W. P. Arnott. 2009. Aerosol light absorption and its measurement: A review. *J. Quant. Spectrosc. Radiat. Transfer* 110 (11):844–78. doi:10.1016/j.jqsrt.2009.02.035.
- Musikhin, S., S. Talebi-Moghaddam, J. C. Corbin, G. J. Smallwood, C. Schulz, and K. J. Daun. 2021. Crumpled few-layer graphene: Connection between morphology and optical properties. *Carbon* 182:677–90. doi:10.1016/j.carbon.2021.06.052.
- Nakayama, T., Y. Kondo, N. Moteki, L. K. Sahu, T. Kinase, K. Kita, and Y. Matsumi. 2010. Size-dependent correction factors for absorption measurements using filter-based photometers: PSAP and COSMOS. *J. Aerosol Sci.* 41 (4):333–43. doi:10.1016/j.jaerosci.2010.01.004.
- Norooz Oliaee, J., N. A. Sabourin, S. A. Festa-Bianchet, J. A. Gupta, M. R. Johnson, K. A. Thomson, G. J. Smallwood, and P. Lobo. 2022. Development of a sub-ppb resolution methane sensor using a GaSb-based DFB diode laser near 3270 nm for fugitive emission measurement. *ACS Sens.* 7 (2):564–72. doi:10.1021/acssensors.1c02444.
- Patimisco, P., G. Scamarcio, F. K. Tittel, and V. Spagnolo. 2014. Quartz-enhanced photoacoustic spectroscopy: A review. *Sensors (Basel)* 14 (4):6165–206. doi:10.3390/s140406165.
- Patrick Arnott, W., H. Moosmüller, C. Fred Rogers, T. Jin, and R. Bruch. 1999. Photoacoustic spectrometer for measuring light absorption by aerosol: Instrument description. *Atmos. Environ.* 33 (17):2845–52. doi:10.1016/s1352-2310(98)00361-6.
- Peña, O., and U. Pal. 2009. Scattering of electromagnetic radiation by a multilayered sphere. *Comput. Phys. Commun.* 180 (11):2348–54. doi:10.1016/j.cpc.2009.07.010.
- Petzold, A., and M. Schönlinner. 2004. Multi-angle absorption photometry – a new method for the measurement of aerosol

- light absorption and atmospheric black carbon. *J. Aerosol Sci.* 35 (4):421–41. doi:10.1016/j.jaerosci.2003.09.005.
- Qiao, S., P. Ma, V. Tsepelin, G. Han, J. Liang, W. Ren, H. Zheng, H. Zheng, and Y. Ma. 2023. Super tiny quartz-tuning-fork-based light-induced thermoelastic spectroscopy sensing. *Opt. Lett.* 48 (2):419–22. doi:10.1364/ol.482351.
- Radeschnig, U., A. Bergmann, and B. Lang. 2024. Optimization of the optical path length amplitude for interferometric photothermal gas and aerosol sensing considering advection: A theoretical study. *J. Appl. Phys* 135 (9): 094501. doi:10.1063/5.0184357.
- Radeschnig, U., M. Knoll, B. Lang, and A. Bergmann. 2021. Photothermal monitor for black carbon mass concentration using a fiber-coupled fabry-pérot interferometer. European Aerosol Conference, Birmingham, UK (Virtual).
- Ramanathan, V., and G. Carmichael. 2008. Global and regional climate changes due to black carbon. *Nature Geosci.* 1 (4):221–7. doi:10.1038/ngeo156.
- Rieker, G. B., J. B. Jeffries, and R. K. Hanson. 2009. Calibration-free wavelength-modulation spectroscopy for measurements of gas temperature and concentration in harsh environments. *Appl. Opt.* 48 (29):5546–60. doi:10.1364/ao.48.005546.
- Rothman, L. S., C. P. Rinsland, A. Goldman, S. T. Massie, D. P. Edwards, J.-M. Flaud, A. Perrin, C. Camy-Peyret, V. Dana, J.-Y. Mandin, et al. 1998. The HITRAN molecular spectroscopic database and HAWKS (HITRAN atmospheric workstation): 1996 Edition. *J. Quant. Spectrosc. Radiat. Transfer* 60 (5):665–710. doi:10.1016/s0022-4073(98)00078-8.
- Schnaiter, F. M., C. Linke, E. Asmi, H. Servomaa, A.-P. Hyvärinen, S. Ohata, Y. Kondo, and E. Järvinen. 2023. The four-wavelength photoacoustic aerosol absorption spectrometer (PAAS-4 $\lambda$ ). *Atmos. Meas. Tech.* 16 (11): 2753–69. doi:10.5194/amt-16-2753-2023.
- Sedlacek, A. J. 2006. Real-time detection of ambient aerosols using photothermal interferometry: Folded jamin interferometer. *Rev. Sci. Instrum* 77 (6):64903. doi:10.1063/1.2205623.
- Sipkens, T. A., A. Boies, J. C. Corbin, R. K. Chakrabarty, J. Olfert, and S. N. Rogak. 2023. Overview of methods to characterize the mass, size, and morphology of soot. *J. Aerosol Sci.* 173:106211. doi:10.1016/j.jaerosci.2023.106211.
- Sipkens, T. A., J. Menser, T. Dreier, C. Schulz, G. J. Smallwood, and K. J. Daun. 2022. Laser-induced incandescence for non-soot nanoparticles: Recent trends and current challenges. *Appl. Phys. B* 128 (4):72. doi:10.1007/s00340-022-07769-z.
- Sorensen, C. M. 2001. Light scattering by fractal aggregates: A review. *Aerosol Sci. Technol.* 35 (2):648–87. doi:10.1080/02786820117868.
- Stylogiannis, A., N. Kousias, A. Kontses, L. Ntziachristos, and V. Ntziachristos. 2021. A low-cost optoacoustic sensor for environmental monitoring. *Sensors (Basel)* 21 (4): 1379. doi:10.3390/s21041379.
- Sullivan, B. T., and J. A. Dobrowolski. 1992. Deposition error compensation for optical multilayer coatings. I. Theoretical description. *Appl. Opt.* 31 (19):3821–35. doi: 10.1364/ao.31.003821.
- Sun, H., L. Biedermann, and T. C. Bond. 2007. Color of brown carbon: A model for ultraviolet and visible light absorption by organic carbon aerosol. *Geophys. Res. Lett.* 34 (17):L178135–L178135. doi:10.1029/2007GL029797.
- Taylor, J. W., J. D. Allan, D. Liu, M. Flynn, R. Weber, X. Zhang, B. L. Lefer, N. Grossberg, J. Flynn, and H. Coe. 2015. Assessment of the sensitivity of core/shell parameters derived using the single-particle soot photometer to density and refractive index. *Atmos. Meas. Tech.* 8 (4): 1701–18. doi:10.5194/amt-8-1701-2015.
- Tian, G., H. Moosmüller, and W. P. Arnott. 2009. Simultaneous photoacoustic spectroscopy of aerosol and oxygen A-band absorption for the calibration of aerosol light absorption measurements. *Aerosol Sci. Technol.* 43 (11): 1084–90. doi:10.1080/02786820903170972.
- Varma, R., H. Moosmüller, and W. P. Arnott. 2003. Toward an ideal integrating nephelometer. *Opt. Lett.* 28 (12):1007–9. doi:10.1364/ol.28.001007.
- Visser, B., J. Röhrbein, P. Steigmeier, L. Drinovec, G. Močnik, and E. Weingartner. 2020. A single-beam photothermal interferometer for in situ measurements of aerosol light absorption. *Atmos. Meas. Tech.* 13 (12):7097–111. doi:10.5194/amt-13-7097-2020.
- Werle, P. 1998. A review of recent advances in semiconductor laser based gas monitors. *Spectrochim. Acta, Part A* 54 (2):197–236. doi:10.1016/s1386-1425(97)00227-8.
- Willets, K. A., and R. P. Van Duyne. 2007. Localized surface plasmon resonance spectroscopy and sensing. *Annu. Rev. Phys. Chem.* 58 (1):267–97. doi:10.1146/annurev.physchem.58.032806.104607.
- Won, Y.-H., O. Cho, T. Kim, D.-Y. Chung, T. Kim, H. Chung, H. Jang, J. Lee, D. Kim, and E. Jang. 2019. Highly efficient and stable InP/ZnSe/ZnS quantum dot light-emitting diodes. *Nature* 575 (7784):634–8. doi:10.1038/s41586-019-1771-5.
- Wu, H., L. Dong, H. Zheng, Y. Yu, W. Ma, L. Zhang, W. Yin, L. Xiao, S. Jia, and F. K. Tittel. 2017. Beat frequency quartz-enhanced photoacoustic spectroscopy for fast and calibration-free continuous trace-gas monitoring. *Nat. Commun.* 8:15331. doi:10.1038/ncomms15331.
- Yang, T., W. Chen, and P. Wang. 2021. A review of all-optical photoacoustic spectroscopy as a gas sensing method. *Appl. Spectrosc. Rev.* 56 (2):143–70. doi:10.1080/05704928.2020.1760875.
- Yu, S., B. J. Drouin, and C. E. Miller. 2014. High resolution spectral analysis of oxygen. Iv. Energy levels, partition sums, band constants, rkr potentials, franck-condon factors involving the X<sup>3</sup> $\Sigma$ g<sup>-</sup>, a<sup>1</sup> $\Delta$ g and b<sup>1</sup> $\Sigma$ g<sup>+</sup> states. *J. Chem. Phys.* 141 (17):174302. doi:10.1063/1.4900510.